Morphology and Charge Transport in Poly(2-methoxy-5-(2′-ethylhexyloxy)-1,4-phenylenevinylene) Films

U. Jeng,*,† C.-H. Hsu,† H.-S. Sheu,† H.-Y. Lee,† A. R. Inigo,*,‡ H. C. Chiu,‡,§ W. S. Fann,‡,§ S. H. Chen,|| A. C. Su,|| T.-L. Lin,⊥ K. Y. Peng,# and S. A. Chen#

National Synchrotron Radiation Research Center, Hsinchu 300, Taiwan; Institute of Atomic and Molecular Sciences, Academia Sinica, P.O. Box 23-166, Taipei 106, Taiwan; Department of Physics and Institute of Polymer Sciences and Engineering, National Taiwan University, Taipei 106, Taiwan; Institute of Materials Science and Engineering and Center for Nanoscience and Nanotechnology, National Sun Yat-sen University, Kaohsiung 804, Taiwan; Department of Engineering and System Science, National Tsing Hua University, Hsinchu 300, Taiwan; and Department of Chemical Engineering, National Tsing Hua University, Hsinchu 300, Taiwan

Received February 21, 2005; Revised Manuscript Received May 13, 2005

ABSTRACT: Structural characteristics of optical quality poly(2-methoxy-5-(2′-ethylhexyloxy)-1,4-phenylenevinylene) (MEH−PPV) films drop-cast from toluene solutions have been examined by use of wide-angle (WAXS) and small-angle X-ray scattering (SAXS) as well as field-emission scanning electron microscopy. For the as-cast film SAXS and WAXS patterns clearly suggest existence of nanodomains of mesomorphic order. Under grazing incidence, both SAXS and WAXS patterns of the as-cast film exhibit impressive uniaxial symmetry with strong scattering along the film normal; however, the corresponding normal-incidence patterns are circularly isotropic, implying in-plane random orientation. A structural model consisting of preferentially uniaxial-oriented nanodomains and disordered matrix is therefore proposed for the as-cast film. Annealing at 210 °C results in disorientation of nanodomains: this decrease in structural asymmetry upon heat treatment correlates well with concomitant changes in charge transport behavior determined from time-of-flight measurements, manifesting dramatically decreased charge mobility as well as transition from nondispersive to dispersive modes.

Introduction

The ease of processing and the flexibility in tailoring of properties via molecular design have made conjugated polymers potential materials for plastic electronics. Among conjugated polymers, poly(1,4-phenylenevinylene) and its derivatives such as poly[2-methoxy-5-(2′-ethylhexyloxy)-1,4-phenylenevinylene] (MEH−PPV) have attracted much attention due to their excellent electroluminescence (EL) properties.[1,2] Nevertheless, the photophysical properties and the final device performance are found to be sensitive to processing parameters such as choice of solvent, solution concentration, spin speed, and heat treatment at elevated temperatures;[3−18] it is most likely that the processing condition determines the film morphology, which in turn affects device efficiency.

In a recent effort to clarify effects of solvent on charge carrier transport behavior,[17] a combination of small-angle X-ray scattering (SAXS) and time-of- flight (TOF) charge mobility measurements was adopted to characterize MEH−PPV films as-cast from toluene or chlorobenzene solutions. The observed electric field and temperature dependence of the nondispersive charge mobility was analyzed on the basis of the Gaussian disorder transport model.[19,20] Results indicated stronger effects from energetic and particularly positional disorder in chlorobenzene-cast film as compared to the toluene-cast counterpart. This is consistent with SAXS observations that the toluene-cast film was of higher structural order and smoother domain−matrix interface than those for the chlorobenzene-cast film. The exact nature of the structural order involved, however, was not examined. In particular, the correlation between morphology and charge transport for as-cast and annealed films has not been established.[11]

It is then interesting to note that there exist variations in conclusions drawn from previous morphological studies regarding the nature of structural order in MEH−PPV films. It had been generally accepted that MEH−PPV films (as prepared by routine spin- or drop-casting procedures) are *amorphous*.[8] In the pioneering study using wide-angle X-ray scattering (WAXS) over MEH−PPV films drop-cast from different solvents and stretched with the aid of a polyethylene substrate, Yang et al.[21] suggested the presence of *crystalline* order (i.e., two-chain orthorhombic unit cell, with $a = 7.1$ Å, $b = 16.1$ Å, and $c = 6.5$ Å) with the coherent length ranging from 50 to 70 Å along the *a*-axis and crystallinity ranging from 20% to 40%. In addition, their WAXS results indicated that MEH−PPV chains tend to lie parallel to film surface; this preferred in-plane backbone arrangement was then correlated to the gain narrowing in the amplified spontaneous emission.[3] More recent WAXS observations as well as polarized light (PLM), scanning (SEM), and transmission electron microscopic (TEM) results of Chen et al.[14−16,18] over a series of PPV derivatives including MEH−PPV confirmed the presence of structural order in drop-cast films, which is more clearly identifiable after heat treatment at an elevated temperature. On the basis of diffuse patterns obtained, the nature of the structural order was designated as *sanidically mesomorphic*, with backbones aggregating

† National Synchrotron Radiation Research Center.
‡ Academia Sinica.
§ National Taiwan University.
|| National Sun Yat-sen University.
⊥ Department of Engineering and System Science, National Tsing Hua University.
Department of Chemical Engineering, National Tsing Hua University.

10.1021/ma050367u CCC: $30.25
Published on Web 06/30/2005

into boardlike entities whereas the alkyl side chains filling the inter-board space. More importantly, grains approximately 10−20 nm in size were identified by means of plane-view TEM and SEM observations, indicating that films are generally heterogeneous at this length scale.

Presented here are results of our recent study using SAXS, WAXS, and SEM for morphological characterization of drop-cast MEH−PPV films both in the as-cast state and after isothermal heat treatment at an elevated temperature of 210 °C. Although structural features observed for the as-cast MEH−PPV films, bearing solvent-induced characteristics that are kinetically trapped during film formation, are inherently metastable, there are two reasons to study them carefully. First, it serves as a basis for understanding the annealed films, which possess thermally equilibrated morphology. Second, application such as ink-jet printing, which is similar to drop-casting method, normally does not involve the annealing process. With a bright X-ray source from synchrotron radiation and the use of grazing-incidence (GI) geometry, the X-ray scattering patterns provide improved resolution of depth and in-plane features that indeed suggest the existence of nanometer-sized domains of mesomorphic order, which are oriented preferentially along film normal in the as-cast state; subsequent annealing at 210 °C results mainly in the randomization of nanodomain orientation. Fractographic features of the MEH−PPV films also support the presence of nanodomains. Accompanying the morphological changes upon heat treatment, results of our time-of-flight measurements indicate dramatic changes in the transport behavior including the order-of-magnitude decrease in charge mobility and the transition from nondispersive to dispersive modes. These changes are interpreted in terms of randomization of nanodomain orientation along the charge transport direction.

Experimental Section

Film Preparation. Nascent MEH−PPV with weight-average molecular mass of ca. 250 kDa, polydispersity index of 6.5 (determined via gel permeation chromatography), and tetrahedral defect density of ca. 2% (determined[22] via nuclear magnetic resonance spectroscopy) was dissolved in toluene (5 mg/mL). Films ca. 3 μm in thickness were prepared via drop-casting at room temperature on glass substrates 2.5 cm × 7 cm in size. To reach adequate surface smoothness for subsequent TOF measurements, the solvent was allowed to vaporize very slowly under a solvent-vapor-rich atmosphere. This condition was maintained for 24 h to result in highly reproducible optical quality films. The films were then placed in dynamic vacuum (i.e., 10^{-6} Torr) to remove the residual solvent for ca. 12 h. For annealed films, the as-cast films were placed in a chamber evacuated to 10^{-3} Torr for another 6 h, followed by purging of dry nitrogen gas to bring the system pressure to slightly above 1 atm. The chamber temperature was then progressively increased to and maintained at 210 °C for 12 h before final cooling to room temperature via reversed steps.

Charge Mobility Measurements. For TOF measurements of charge carrier mobility, MEH−PPV films were top-coated with a layer (ca. 100 nm in thickness) of Au via thermal evaporation and shadow masking for an active area of 4 mm^2. Details of instrumentation and experimental procedures are the same as those reported previously.[10] Measurements were then made on four different specimens from two different solution batches; the results were highly reproducible even when repeated a month later.

Grazing-Incidence Wide-Angle X-ray Scattering. GI-WAXS measurements were conducted on the 8-circle diffractometer at the wiggler beamline BL17B of the Taiwan light source at the National Synchrotron Radiation Research Center (NSRRC). Using an X-ray beam of 1.240 Å and an incident angle of 0.30°, we could increase the beam path inside the sample films by 2 orders of magnitude, as compared to the case of normal incidence. With the greatly enhanced beam path and the high-flux synchrotron X-ray source, we collected WAXS data in the in-plane and the depth (z) directions of the films, respectively. The low divergence in the vertical direction of the synchrotron beam allowed us to scan data with a point detector in a wide Q range (0.1−4.5 Å^{-1}) along the z direction; for the in-plane direction, we scanned from ca. 0.3 to 4.0 Å^{-1}. Here the scattering vector $Q = 4\pi \sin(\theta/2)/\lambda$ is defined by the scattering angle θ and the X-ray wavelength λ. For background subtraction, WAXS pattern from the glass substrate was measured. Two-dimensional (2D) GI-WAXS patterns were recorded with an imaging plate (IP) on the X-ray powder diffractometer (beamline BL17A at NSRRC) at a longer wavelength of 1.327 Å. To obtain full range (2π) scattering patterns on IP with grazing incident geometry, we detached each film specimen from the glass substrate and folded it into layers ca. 120 μm in total thickness and ca. 5 mm × 5 mm in area.

Small-Angle X-ray Scattering. For the SAXS study, we used free-standing films detached from glass substrates. Measurements were made using an 8 m SAXS instrument at the National Tsing Hua University, with the film surface oriented either perpendicular or nearly parallel to the incident beam. With a pencil-like beam (1.540 Å in wavelength and 1 mm in diameter), the SAXS instrument covered a Q range of 0.008−0.2 Å^{-1}. The data collected using a 2D multiwired area detector were corrected for sample transmission, background, detector sensitivity, and circularly averaged (isotropic scattering cases) or striped averaged (asymmetrical scattering cases) for the one-dimensional (1D) scattering intensity $I(Q)$. Further instrumental details have been given elsewhere.[17]

Scanning Electron Microscopy. Topographic features of cryogenically fractured surfaces of as-cast and annealed MEH−PPV films were examined via secondary electron images (SEI) obtained by use of a field-emission scanning electron microscope (JEOL JSM-6330TF) under an accelerating voltage of 10 kV. To avoid charging, specimens were sputter-coated with a thin layer of gold prior to SEM observations.

Results and Discussion

Wide-Angle X-ray Scattering. The GI-WAXS patterns showed no sharp diffraction peaks; only halos are observed in both the in-plane and depth directions of the film (cf. Figure 1a), indicating general absence of large domains of three-dimensional (3D) positional order in the film. It is nevertheless convenient to interpret the diffraction pattern in terms of the concept of nanocrystalline domains,[23,24] which has been adopted to interpret medium-range order (MRO) in materials such as "amorphous" silicon that lie somewhat beyond the borderline of traditional definition of crystals. From the widths of the halos, the size of chain-packed MEH−PPV nanocrystalline domain is estimated as ca. 20 Å for both the Q = 1.01 and 1.48 Å^{-1} halos (which correspond to d spacing values of 6.3 and 4.3 Å, respectively) and 100 Å for the 0.26 Å^{-1} halo (which corresponds to 24 Å in d spacing). The positional order does not extend beyond ca. 4 d spacing values and is indeed medium range at most.

Scattering profiles along the depth and the in-plane directions are similar in shape but much stronger in intensity for the former case. This suggests structural anisotropy along the film normal. To quantitatively compare the scattering intensities in the two directions, we further correct the WAXS data for sample transmission and beam path length, as detailed in the Appendix.

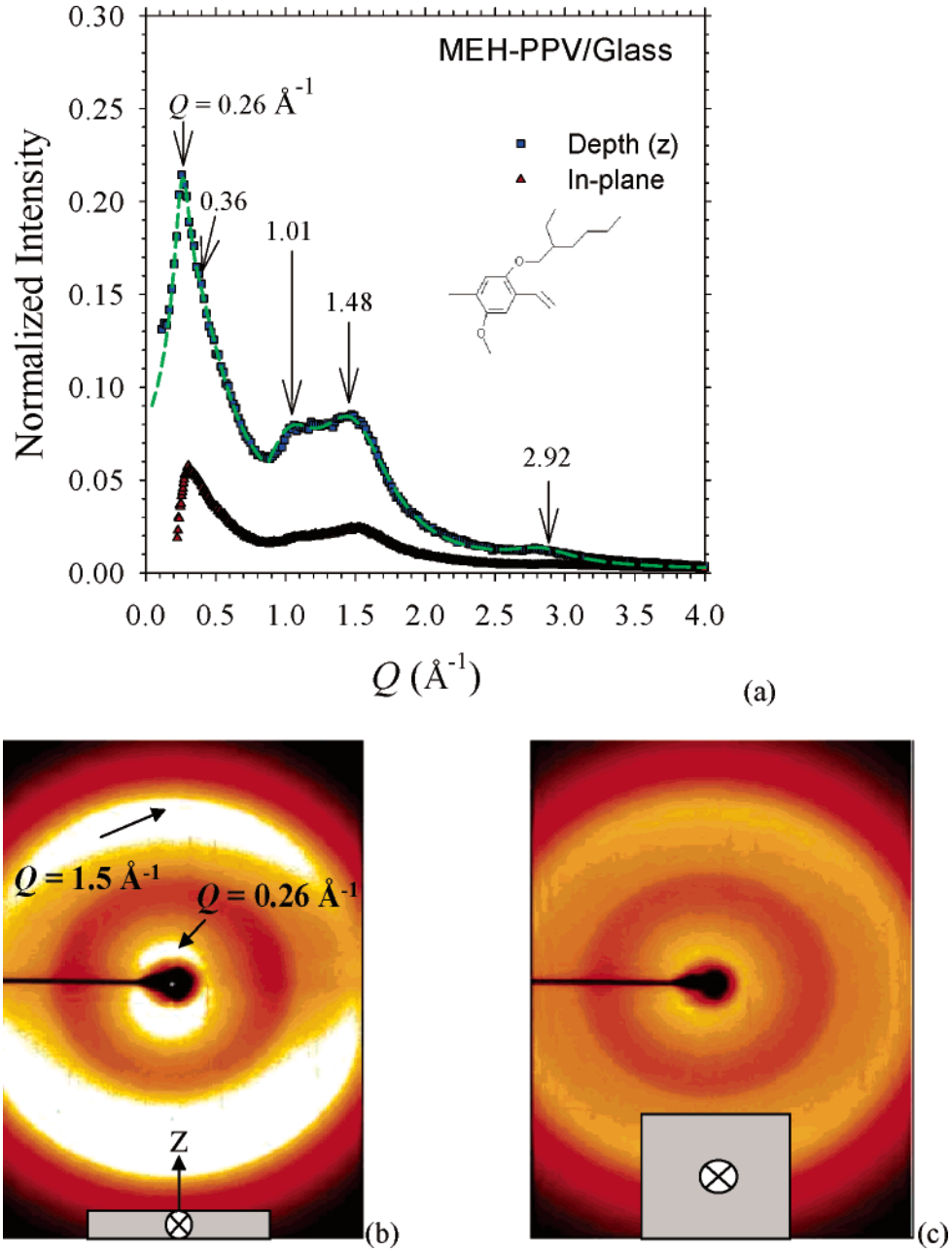

Figure 1. (a) Grazing-incidence WAXS data collected in the in-plane (triangles) and depth (rectangles) directions for the toluene-cast film of MEH−PPV on a glass substrate. The data in the depth direction are fitted (dashed curve) using five Lorentzian functions centering at 0.26, 0.36, 1.01, 1.48, and 2.92 Å^{-1}. The in-plane WAXS data are corrected for intensity comparison (see Appendix). Also shown are two-dimensional WAXS patterns for the MEH−PPV film detached from the substrate, obtained under grazing incidence (b) or normal incidence (c). The gray rectangle in each image indicates the film orientation whereas the cross represents the incident beam. The strong scattering in the surface-normal direction (z) in (b) corresponds to the depth structural information on the film.

The asymmetrical scattering pattern, emphasized in the depth direction, is better illustrated by the 2D scattering image (cf. Figure 1b) taken from the free-standing film at quasi-parallel incidence. In contrast, the corresponding normal-incidence WAXS pattern (cf. Figure 1c) exhibits Debye−Scherrer conelike features of circular symmetry, indicating that there is no preference in the in-plane orientation.

The observations of nanometer-sized domains and in-plane isotropy are consistent with previous PLM, TEM, and WAXS results[14−16,18] of high beam-incidence angles, which had led to the conclusion that the as-cast films are largely isotropic and disordered in the in-plane direction. We note that Yang et al.[21] have previously indicated a similar asymmetry structure in the depth direction from their 2D WAXS pattern of near-parallel incidence over a stretched MEH−PPV film cast from tetrahydrofuran. This uniaxial structural anisotropy, also identified[17] for the MEH−PPV film cast from chlorobenzene, is therefore very likely a general feature qualitatively shared among as-cast films. Nevertheless, there may exist delicate differences in quantitative aspects of nanodomain development and roughness of the nanodomain/matrix interface under different processing conditions.[17]

Medium-Range Order within Nanodomains. For comparison with the crystalline model proposed by Yang et al.,[21] characteristics lengths in Figure 2a may be conveniently dubbed as "unit cell" parameters with a = 4.3 Å, b = 24.2 Å, and c = 6.3 Å. With these lengths

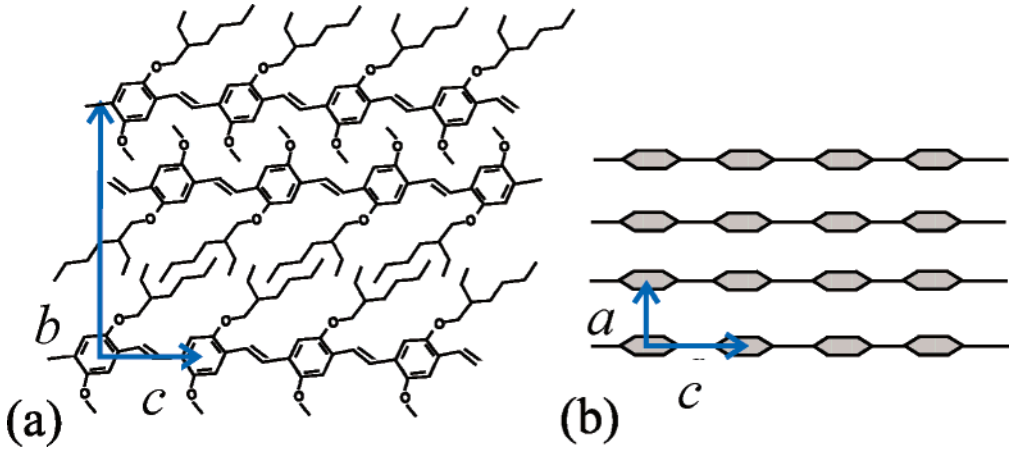

Figure 2. Schematic model for the local packing of MEH−PPV chains, in which characteristic lengths c represents the monomeric repeat along the MEH−PPV backbone, b the bilayer spacing, and a the interbackbone spacing perpendicular to the **b** × **c** plane. Two orthogonal views are given: one shows the bilayer normal in parallel to the film normal (a), and the other shows benzene ring planes lying parallel to the film surface (b). Note that the depicted positional order extends only for several characteristic lengths in each direction, as estimated from the widths of the corresponding scattering halos.

we build a locally ordered structure to reflect the scattering characteristics. Shown in parts a and b of Figure 2 are the two orthogonal views (**b** × **c** and **a** × **c**, respectively) of locally ordered chain packing, with characteristic lengths $c = 6.3$ Å assigned to monomeric repeats along the backbone of MEH−PPV, $b = 24.2$ Å assigned to the bilayer spacing of two neighboring MEH−PPV chains (assumed to be in all-trans, planar configuration) arranged in a face-to-face manner, and $a = 4.3$ Å attributed to the interbackbone spacing in the direction normal to the coplanar phenylene rings.

Compared to the previous model of crystalline order (i.e., two-chain orthorhombic unit cell, with $a = 7.1$ Å, $b = 16.1$ Å, and $c = 6.5$ Å) proposed by Yang et al.,[21] the present model is greater in layer spacing (24 vs 16 Å) and in in-layer interbackbone spacing (4.3 vs 3.55 Å). The greater b value observed here matches with the bilayer spacing of MEH−PPV, ca. 11 Å in width, contributed by a benzene ring plus the two side chains. This bilayer ordering may originate from a dimeric interaction of MEH−PPV chains in the solution state, as previously suggested by Shi et al.[5] It may be envisioned that, during solvent evaporation and film formation, these dimers aggregate transversely (i.e., stack along the b-axis in Figure 2 to connect the aromatic backbones and aliphatic side chains) into a *locally* planar bilayer structure.

It is then interesting to note that a closer scrutiny at the scattering profile in Figure 1a reveals that the bilayer peak centering at 0.26 Å^{-1} is in fact overlapping with a neighboring peak centering at 0.36 ± 0.035 Å^{-1} (of comparable intensity contribution), which corresponds to a smaller layer spacing of 17.5 ± 1.5 Å. In this latter case, the alkyl side chains in the structural model of Figure 2a are envisioned to make out-of-plane tilt to fit the shorter bilayer spacing. The observed WAXS pattern is therefore considered a result of the two types of bilayer packing (24.2 vs 17.5 Å in spacing) coexisting in the film. The former is in fact a solvent-induced transient structure that bows away to the latter upon heat treatment at 210 °C, as to be delineated in a later subsection. This latter structure is reasonably close to the b value (16.1 Å) reported for the crystalline model of Yang et al.[21] or the layer spacing (15.3 Å) reported for the sanidically mesomorphic order[15] of MEH−PPV.

Anisotropy in the As-Cast Film. There is one more point to be made on the basis of Figure 1a: the much higher intensity at $Q = 0.26$ Å^{-1} in the depth direction, compared to that in the in-plane direction, indicates that the bilayers within the MRO nanodomains prefer to stack along film normal (Figure 2a). From the 0.26 Å^{-1} peak intensities, we extract an orientation parameter $p = (I_d - I_i)/(I_d + I_i) =$ ca. 0.6, where I_d and I_i represent peak intensities in the depth and the in-plane directions, respectively. This preferred bilayer staking along the film normal is attributed to the preference of alkyl side chains toward the air−liquid interface (thereby reducing surface tension), which serves to "guide" (via "amphophilic" nature of MEH−PPV, in which incompatibility exists between the aromatic backbone and the covalently attached alkyl side chains) the alignment of subsequently assembled domains upon gradual depletion of solvent through diffusion and evaporation along the film normal.

In recent morphological studies[25,26] of poly(9,9-di-*n*-octyl-2,7-fluorene), in which the crystalline order within the nanodomains allows for clear identification of nanodomain orientation via selected-area electron diffraction, conclusive evidence for orientation of nanodomains has been reported. In a more recent study of a related polyfluorene derivative with branched side chains, Jung et al.[27] have provided conclusive evidence of carbon K-edge soft X-ray absorption spectroscopy in support of this attribution. In the present as-cast MEH−PPV film, the scattering arc centered around $Q = 0.26$ Å^{-1} in the vertical direction (Figure 1b) signifies this uniaxial orientation, with the spread angle of the arc reflecting a nonperfect alignment of the MEH−PPV nanodomains in the surface normal direction.[28] It is therefore indeed plausible that this tendency of preferred orientation, observed via diffraction or spectroscopic evidences for different conjugated polymers grafted with alkyl side chains, is likely a general phenomenon attributable to the consistent presence of alkyl side chains in these polymers. Complementary evidence from surface spectroscopy would be preferable, but this is beyond the scope of present work.

Small-Angle X-ray Scattering. With the incident beam nearly parallel to the film, the SAXS pattern (Figure 3a) for the free-standing film shows more impressively the uniaxial symmetry in the direction

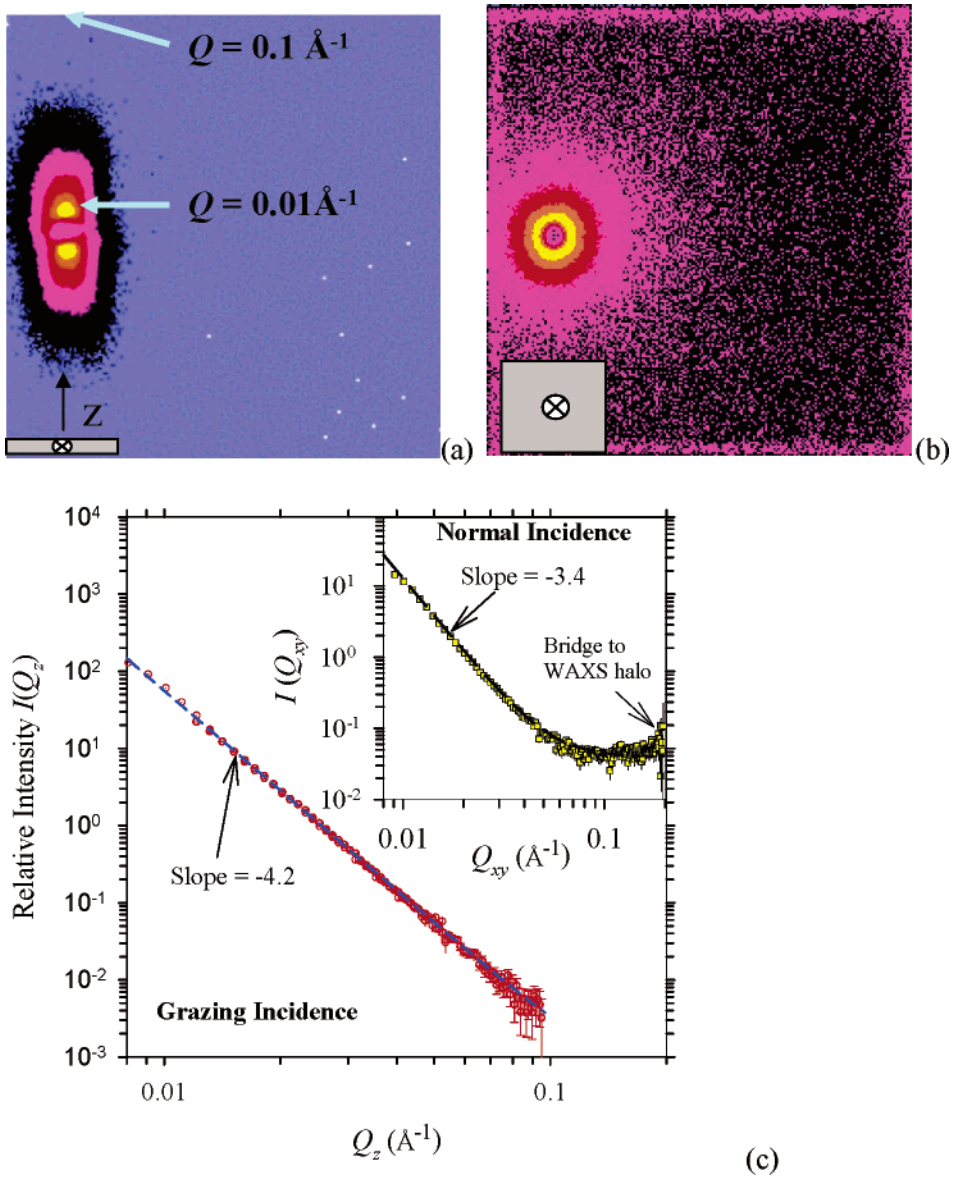

Figure 3. SAXS patterns of the MEH−PPV film detached from the substrate, obtained at grazing incidence (a) and normal incidence (b). The rectangle and the cross at the bottom of each image indicate the film orientation and the incident beam direction, respectively. (c) SAXS profile obtained along the depth direction (z) in (a) exhibits a power-law scattering characteristic, which may be fitted (dashed line) to give a slope $r = -4.2$. The inset shows the SAXS profile obtained from (b), which also exhibits a power-law feature (dashed line) with $r = -3.4$.

perpendicular to the film surface (depth direction). The pattern, similar to that for polymer fibers of uniaxial oriented domains,[29] has much stronger density fluctuations along the depth direction of the film than in the in-plane direction. On the other hand, with the incident beam perpendicular to the film, the SAXS pattern is circular isotropic (Figure 3b), implying a symmetrical structure in the in-plane direction. This strong anisotropy scattering in the depth direction and circularly symmetrical scattering in the in-plane direction is consistent with the WAXS result.

In Figure 3c, both the depth SAXS and the in-plane SAXS profiles obtained from parts a and b of Figure 3, respectively, exhibit the power law scattering characteristic $I(Q) \propto Q^r$, with $r = -4.2$ for the depth SAXS and -3.4 for the in-plane SAXS. In the surface fractal model,[33] scattering dominated by a fractal surface morphology is described by $I(Q) \propto Q^{-(6-D_s)}$ with the fractal dimension D_s between 2 and 3, leading to possible p values between -4 and -3. For $r < -4$, surfaces can be characterized further by including surface roughness.[30] In our case, the $r = -4.2$ observed in the depth direction for the MEH−PPV film implies that the SAXS intensity is contributed by largely smooth surfaces of small roughness. In contrast, the scattering power of $r = -3.4$ for the in-plane SAXS (corresponding to $D_s = 2.6$) implies that the scattering is dominated by surface facets of fractal nature. It should be noted here that the term surface (as inherited from the original work[31]) corresponds to domain/matrix interface for our SAXS study of detached films in transmission mode.

Morphology of the As-Cast Film. With the WAXS data providing information short-range chain packing and SAXS on local density fluctuations up to mesoscale, we have sufficient information to build a structural picture for MEH−PPV films studied. In Figure 4a, we propose a mesoscale structure for MEH−PPV aggregates (or nanodomains) composed of locally stacked MEH−PPV chains, as shown in Figure 2. From the top view of the ordered domain (right-hand side of Figure

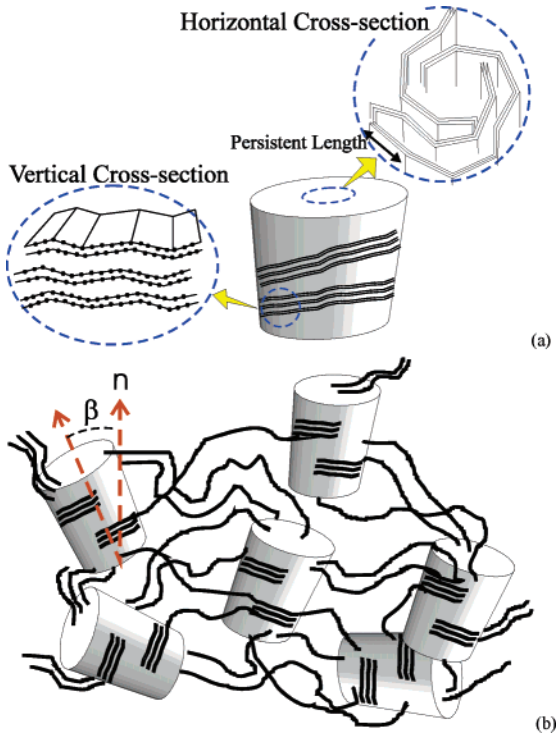

Figure 4. (a) Structural model for the ordered nanodomains. The cylindrical shape adopted here is encouraged by the FE−SEM images for the domains. Depicted on the right is the horizontal cross section of the nanodomain, exhibiting fractal-like coiling of the MEH−PPV backbones at scales greater than the persistent length (indicated by the two-way arrow). Illustrated on the left is the bilayer packing with uniaxial symmetry. (b) Cartoon for spatial arrangement of nanodomains that are connected via disordered regions of random-coiled MEH−PPV chains. Note that the lines representing the amorphous chains are only for a schematic view. The nanodomains tend to orient preferentially along the surface normal (n) with a mean spread angle β.

4a), we envisage the passage of MEH−PPV backbones (regulated by the persistent length of ca. 13 nm)[32] through nanodomains of ordered packing with irregular, fractal-like interfaces. This accounts for the isotropic WAXS and SAXS patterns observed with normal incident beam. When we take a side view of the ordered domain (left-hand side of Figure 4a), smoother interfaces dictated by the bilayer structure are observed, reflecting the power law scattering of $r = -4.2$ in SAXS and the bilayer peak in WAXS. In the expanded view (cf. Figure 4b), we incorporate the spread angle β of the domain orientation, with disordered MEH−PPV chains filling the interdomain space. The anisotropic orientation of ordered domains in Figure 4b reflects approximately the orientation parameter $p = 0.6$. Overall, the ordered domains distribute uniformly inside the film, leading to a homogeneous depth density profile after averaging the densities of the ordered and amorphous areas in the corresponding in-planes.

It should be emphasized that this anisotropic orientation appears to be a general feature qualitatively shared by films prepared from aromatic solvents. The present model therefore bears some practical significance, as most of the reported device fabrication procedures do not include a high-temperature annealing step; more importantly, it serves as a basis for the discussion of thermally equilibrated film morphology presented below.

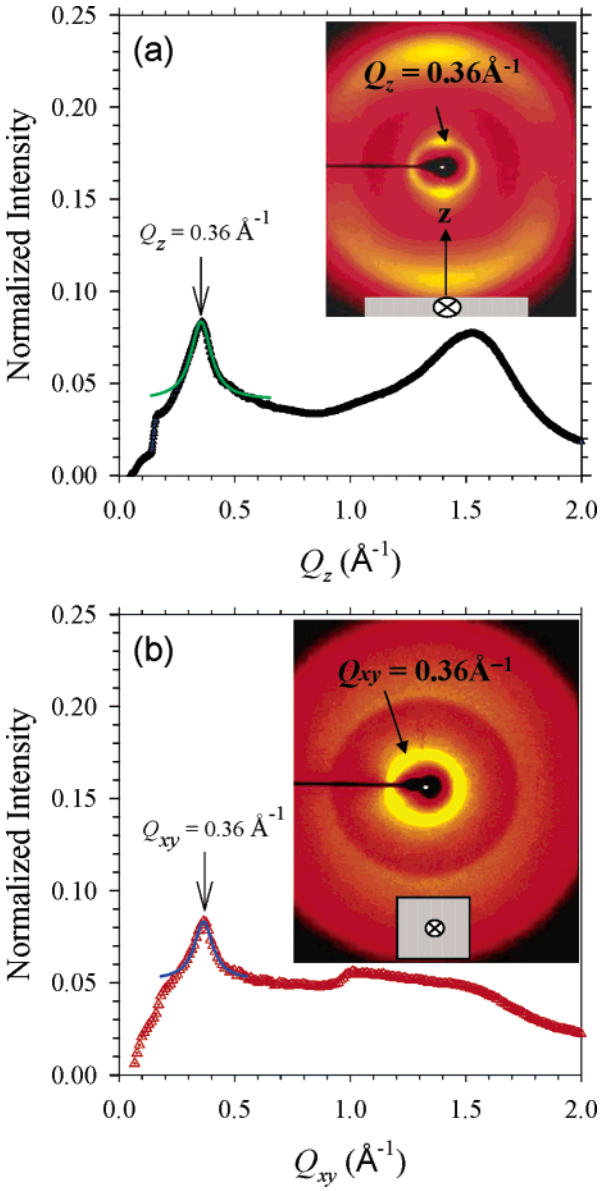

Figure 5. (a) Grazing-incidence WAXS profile in the depth direction, obtained from the 2-D WAXS pattern (inset, showing weaker and yet still significant anisotropy along film normal), of the heat-treated MEH−PPV film. (b) Normal-incidence WAXS profile extracted from the corresponding 2-D WAXS pattern (inset, showing clear in-plane isotropy) for the heat-treated MEH−PPV film. Also given are Lorentzian fits (solid curves) to the peak of bilayer order at 0.36 Å^{-1}.

Morphology of Thermally Equilibrated Film. Structural features observed above for the as-cast MEH−PPV films, bearing solvent-induced characteristics that are kinetically trapped during film formation, are inherently metastable. This is most clearly demonstrated by annealing at 210 °C. In Figure 5a (inset), the WAXS image taken under a grazing incident beam for the annealed free-standing film of MEH−PPV demonstrates the dramatic effect of annealing on the film structure. The layering features composed of two overlapping arcs in the depth direction of the as-cast film (see Figure 1b) converge into a single spacing of 17.5 Å (at $Q = 0.36 \pm 0.02$ Å^{-1}) and spread into a circle for this case of annealed film. Correspondingly, the normal-incidence WAXS pattern (cf. Figure 5b) shows Debye−Scherrer ring at the same $Q = 0.36$ Å^{-1} position. Clearly, the structure of the MEH−PPV film becomes more

isotropic upon annealing. In addition, the transient bilayer packing (24.2 Å in spacing) in the as-cast film transforms into its thermodynamically favored counterpart (17.5 ± 1.0 Å in spacing) during annealing.

From the widths of the 0.36 $Å^{-1}$ peaks fitted using Lorentzian profiles (solid curves in Figure 5a,b), we estimate that the coherent length of the bilayers amounts to ca. 125 and 110 Å in the depth and the in-plane directions, respectively. These are comparable to that (ca. 100 Å) obtained for the as-cast film. It therefore follows that annealing at 210 °C serves mainly to randomize the kinetically oriented nanodomains in the film with insignificant changes in the domain size, although minor adjustment of the MRO within nanodomains indeed results in a converged layer spacing of 17.5 Å. The randomized reorientation of nanodomains in the annealed film may also be perceived by the relative intensity changes in the two peaks at $Q = 0.36$ $Å^{-1}$ (bilayer spacing along the b-axis) and 1.5 $Å^{-1}$ (interbackbone distance along a-axis) (cf. Figures 1 and 5). Similar structural characteristics for toluene-cast MEH−PPV films annealed briefly (5 min) at 230 °C were observed by selected-area electron diffraction in a recently study by Chen et al.[15] Although not given here, we have also made similar studies on MEH−PPV films cast from chlorobenzene: the general feature of anisotropy along depth direction persists in the as-cast film, with only minor differences in structural details. Annealing of the chlorobenzene-cast film at 210 °C results in essentially the same structure as that presented here for the toluene-cast annealed film.

It is therefore concluded that, aside from minor structural reorganization within the nanodomains toward the thermodynamically favored bilayer packing with lamellar spacing of 17.5 Å, the main effect of heat treatment at an elevated temperature is the disruption of orientation of nanodomains during film formation upon solvent evaporation. Both the rotation of side chains for shorter bilayer spacing and the reorientation of the ordered domains for a more isotropic structure, proposed here for the structural changes of the MEH−PPV film upon isothermal annealing, are consistent with the DSC results of Chen et al.,[15] in which the transformation was shown thermally weak.

Charge Transport. Intra- and interchain hopping processes govern charge transport in conjugated polymers. In TOF measurements, a nanosecond light pulse produces a thin layer of charge carriers on one side of the conjugated polymer film of thickness L. The carriers move through the film under an applied electric field (E), with transit time τ. The mobility of the dominate charge carriers (in the case of MEH−PPV, holes) is thus defined as $\mu = LE/\tau$. In the ideal case of charge carriers moving with constant velocity in a homogeneous body, the photocurrent transients obtained in TOF measurements should show step changes. In reality, the dispersion of charge carrier velocity due to presence of energetic and spatial heterogeneities result in deviations from the ideal step shape.[10,17]

Accompanying the nanodomain orientation randomization upon annealing, there are clear changes in the charge transport properties of the annealed film, as demonstrated by TOF results. Figure 6 shows the hole transport characteristics for the MEH−PPV film in linear and log scale. For the as-cast films the hole transient exhibits nondispersive behavior which has the initial spike, plateau, and a long tail after the transit

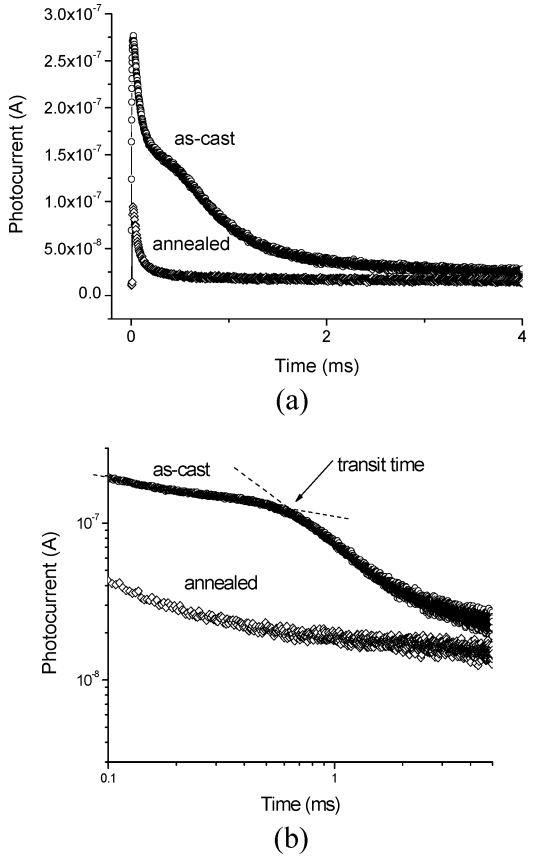

Figure 6. Photocurrent measured by the time-of-flight technique for as-cast and annealed MEH−PPV films for the electric field 1.5×10^5 V/cm. The transit time τ for the as-cast film is determined from the intersection of the asymptotes for the plateau and the declining regions.

time. The mobility observed at the field of 1.5×10^5 V/cm is $(4 \pm 0.05) \times 10^{-6}$ $cm^2/(V\ s)$. Detailed discussion on the nondispersive mobility with respect to field and temperature effects has been given previously.[17] Features of nondispersive hole transient were drastically altered after annealing. In annealed films, there are not only a qualitative change from nondispersive to dispersive characteristics but also a quantitative decrease in hole mobility in the transport behavior. Despite numerous attempts using similarly annealed samples from different solution batches, we could not obtain a clearly defined transit time from the TOF curves.[11] These results illustrate unambiguously dramatic changes in charge transport behavior with the concomitant loss of nanodomain orientation along the depth direction. This leads us to propose that the uniaxial symmetry due to alignment of the nanodomains in the as-cast films is responsible for the nondispersive through-thickness charge transport. The more isotropic film morphology due to randomized nanodomain orientation changes the transport mode from a quasi-1D picture to a 3D hopping process. This proposed interpretation is based on the assumption that the hopping of charge carriers across ordered neighboring chains is easier than along a chain of broken conjugations. Although this assumption appears reasonable, it is yet to be confirmed via carefully designed experiments. Nevertheless, preliminary results[33] from in-plane space charge limited current measurements for flow-aligned MEH−PPV film embedded between parallel gold electrodes indeed suggest higher (by orders of magnitude) hole mobility than

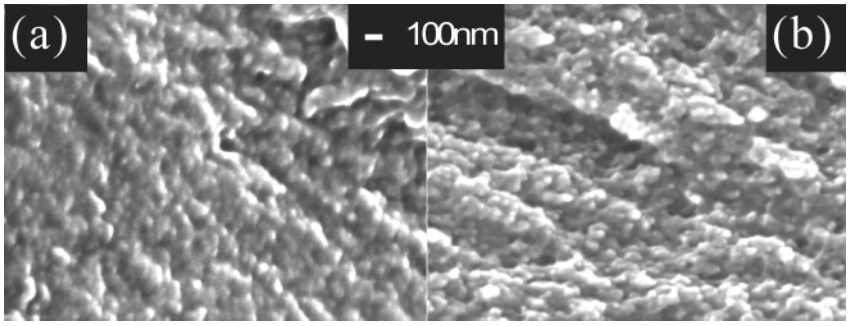

Figure 7. Representative secondary electron images demonstrating topographic features of cryogenically fractured (a) as-cast and (b) annealed MEH−PPV films. Note that particle-like features (ca. 40−100 nm in size) correspond to better-bonded nanodomains, which remained connected during cracking.

typical through-thickness values obtained from the TOF method.

Fractographic Features. As a final piece of evidence in support of the proposed nanodomain picture for the inherent heterogeneity in MEH−PPV films, through-thickness fractographic features of cryogenically fractured films are presented in Figure 7. The secondary electron images indicate predominance of particle-like features on the fracture surface for both the as-cast (Figure 7a) and the annealed (Figure 7b) films. The size of the particle-like entities lies in the range of 40−100 nm, indicating that they are composed of clusters of nanodomains that remain adhered during cracking. This is consistent with previous SEM observation (Figure 4c in ref 15) that MEH−PPV nanodomains are not strongly bonded and tend to crack into clusters ca. 100 nm in size. The fact that fractographic features before and after annealing remain largely similar is consistent with our conclusion that the main difference in film morphology upon annealing is the randomization of nanodomain orientation. We note, however, that the reorganization of the medium-range order within nanodomains, although considered "comparatively minor" in the realm of present discussion of charge transport behavior, may in fact bear major significance in the red-shifted emission at 640 nm upon heat treatment, as a result of efficient funneling of excitonic energy through long-range resonance energy transfer.[16,34−36]

Comments on the Absence of Long-Range 3D Positional Order. We have avoided the use of *crystalline* order in describing the film structure but adopting terms such as medium-range or mesomorphic order instead. Reasons behind this are multiple: the most direct one is that the diffraction patterns obtained do not reflect the existence of long-range 3D positional order, as presented in previous subsections. Crystalline order is more clearly identifiable in polyfluorenes,[25,26,37,38] for which clear [00*l*] zone patterns and fiber patterns were obtained and indexed. Despite our extensive efforts, this is never achieved in the case of MEH−PPV; the best we (and others, such as Yang et al.) have obtained is fiber patterns of very limited number of reflection arcs. These do not constitute supports to crystalline order. Results of extensive differential scanning calorimetry (DSC) scrutinies[15] also showed no discernible thermal event for the melting of such a hypothetical possibility of crystalline order. One of the reasons for the difficulty in developing long-range 3D order in MEH−PPV could be the branched nature of the side chains. As pointed out by Tanto et al.,[39] the ethylhexyl group is basically chiral with an asymmetric carbon center. During the synthesis of MEH−PPV, chirality was generally left uncontrolled, resulting in enatiomeric mixture of randomly distributed ethylhexyl groups of opposite chirality (and hence inherent disorder) along the backbone.

Concluding Remarks

In summary, on the basis of detailed X-ray scattering evidences for as-cast and annealed MEH−PPV films, we propose a physical picture that links film morphology to charge transport behavior in a qualitative way. Of central significance is the asymmetrical orientation of the chain-packed nanodomains of medium-range order, which are dispersed in the matrix of disordered chain packing. In the as-cast film, the nanodomains are oriented preferentially along film normal, endowing efficient, nondispersive, pseudo-1D charge transport characteristics. Aside from minor structural reorganization within the nanodomains, thermal equilibration at an elevated temperature results mainly in disorientation of the nanodomains, which brings the charge transport process back to a more general 3D process and hence broadened distribution of transient time in the vertical direction.

Although we have suggested an apparent correlation between the ordered domains (responsible mainly for interchain charge hopping) and the charge transport properties using the as-cast and the annealed MEH−PPV films, little understanding on the role of the "amorphous" matrix (specifically, the mesh heterogeneity of the chains) in the charge transport properties. To separate the effects of the ordered domains and the amorphous network, we need more sophisticated sample preparation and scattering or microscopic techniques. A possible way may be to prepare a completely amorphous film manipulated by, for instance, electrical field and probe, using the small-angle scattering technique, the conformational changes in the mesh morphology of the chains upon isothermal annealing.

Acknowledgment. We thank Professor J. H. Hsu at NSYSU for inspiring discussion. Financial support from the Ministry of Education (Grant 91-E-FA04-2-4A) and National Science Council (Grant 93-2120M-002-009) is gratefully acknowledged.

Appendix

In WAXS, the scattering intensity is proportional to the transmission $T = \exp(-\mu l)$, where μ is the linear X-ray absorption coefficient of the film and l is the effective sample thickness (beam path length of the sample), namely, $I(Q) \propto l \exp(-\mu l)$. For a film of a thickness t, $l = (t/\sin\theta_{in} + t/\sin\theta_{out})$, with θ_{in} and θ_{out}

for the incident and exit angles in the scattering plane, respectively. In grazing incident WAXS where $\theta_{out} \gg \theta_{in}$ in most of the Q range measured, we have $l \approx t/\sin \theta_{in}$ in the surface normal direction. In the in-plane direction, $l = 2t/\sin \theta_{in}$, when we use $\theta_{out} = \theta_{in}$ for in-plane WAXS scanning. Therefore, the normalization factor for the transmission and effective sample thickness of the in-plane WAXS is larger than that for the depth-WAXS by a factor of $R \approx 2 \exp(-\mu t/\sin \theta_{in})$. The value of $\mu = \rho\sigma_a$ can be calculated from the density $\rho = 1.06$ g/cm^3 of the film derived from the X-ray total reflection edge $Q_c = 2(4\pi\rho b)^{1/2}$ and the X-ray absorption σ_a of the molecules from the molecular formula of MEH−PPV and the X-ray energy used. For intensity comparison, we can divide the scattering intensity obtained in the in-plane direction by the R factor. With the calculated μ value of 2.58 cm^{-1} (for $\lambda = 1.240$ Å) and the incident angle of 0.3° used, $R \approx 1.7$. In this study, R is calculated for each Q value without the $\theta_{out} \gg \theta_{in}$ approximation.

Supporting Information Available: WAXS results of as-cast and annealed films from chlorobenzene solution. This material is available free of charge via the Internet at http://pubs.acs.org.

References and Notes

(1) Friend, R. H.; Gymer, R. W.; Holmes, A. B.; Burroughes, J. H.; Marks, R. N.; Taliani, C.; Bradley, D. D. C.; DosSantos, D. A.; Bredas, J. L.; Logdlung, M.; Salaneck, W. R. *Nature (Landon)* **1999**, *397*, 121.
(2) Dai, L.; Winkler, B.; Dong, L.; Mau, A. W. H. *Adv. Mater.* **2001**, *13*, 915.
(3) Hide, F.; Diaz-Garcia, M. A.; Schwartz, B. J.; Anderson, M. R.; Pei, Q.; Heeger, A. J. *Science* **1996**, *273*, 1833.
(4) Nguyen, T. Q.; Doan, V.; Schwartz, B. J. *J. Chem. Phys.* **1999**, *110*, 4068.
(5) Shi, Y.; Liu, J.; Yang, Y. *J. Appl. Phys.* **2000**, *87*, 4254.
(6) Liu, J.; Shi, Y.; Ma, L.; Yang, Y. *J. Appl. Phys.* **2000**, *88*, 605.
(7) Nguyen, T. Q.; Martini, I. B.; Liu, J.; Schwartz, B. J. *J. Phys. Chem. B* **2000**, *104*, 237.
(8) Lee, T. W.; Park, O. O. *Adv. Mater.* **2000**, *12*, 801.
(9) Nguyen, T. Q.; Yee, R. Y.; Schwartz, B. J. *J. Photochem. Photobiol.* **2001**, *144*, 21.
(10) Inigo, A. R.; Tan, C. H.; Fann, W. S.; Huang, Y. S.; Perng, G. Y.; Chen, S. A. *Adv. Mater.* **2001**, *13*, 504.
(11) Tan, C. T.; Inigo, A. R.; Fann, W. S.; Wei, P. K.; Peng, G. Y.; Chen, S. A. *Org. Electron.* **2002**, *3*, 81.
(12) Yu, L. S.; Tseng, H. E.; Lu, H. H.; Chen, S. A. *Appl. Phys. Lett.* **2002**, *81*, 2014.
(13) Liu, J.; Guo, T. F.; Yang, Y. *J. Appl. Phys.* **2002**, *91*, 1595.
(14) Chen, S. H.; Su, A. C.; Huang, Y. F.; Su, C. H.; Peng, G. Y.; Chen, S. A. *Macromolecules* **2002**, *35*, 4229.
(15) Chen, S. H.; Su, A. C.; Chou, H. L.; Peng, K. Y.; Chen, S. A. *Macromolecules* **2004**, *37*, 167.
(16) Chen, S. H.; Su, A. C.; Han, S. R.; Chen, S. A.; Lee, Y. Z. *Macromolecules* **2004**, *37*, 181.
(17) Inigo, A. R.; Chiu, H. C.; Fann, W. S.; Huang, Y. S.; Jeng, U.; Lin, T. L.; Hsu, C. H.; Peng, K. Y.; Chen, S. A. *Phys. Rev. B* **2004**, *69*, 075201.
(18) Chen, S. H.; Su, C. H.; Su, A. C.; Chen, S. A. *J. Phys. Chem. B* **2004**, *108*, 8855.
(19) Borsenberger, P. M.; Pautmeier, L. T.; Bassler, H. *Phys. Rev. B* **1992**, *46*, 12145.
(20) Bässler, H. *Phys. Status Solidi B* **1993**, *175*, 15.
(21) Yang, C. Y.; Hide, F.; Diaz-Garcia, M. A.; Heeger, A. J.; Cao, Y. *Polymer* **1998**, *39*, 2299.
(22) Inigo, A. R.; Chiu, H. C.; Fann, W.; Huang, Y. S.; Jeng, U. S.; Hsu, C. H.; Peng, K. Y.; Chen, S. A. *Synth. Met.* **2003**, *139*, 581.
(23) Cheng, J. Y.; Gibson, J. M.; Jacobson, D. C. *J. Mater. Res.* **2001**, *16*, 3030.
(24) Cheng, J. Y.; Gibson, J. M.; Baldo, P. M.; Kestel, B. J. *J. Vac. Sci. Technol. A* **2002**, *20*, 1855.
(25) Brulet, A.; Boue, F.; Keller, P.; Davidson, P.; Strazielle, C.; Cotton, J. P. *J. Phys. II* **1994**, *4*, 1033.55.
(26) Chen, S. H.; Su, A. C.; Su, C. H.; Chen, S. A. *Macromolecules* **2005**, *38*, 379.
(27) Jung, Y.; Cho, T. Y.; Yoon, D. Y.; Frank, C. W.; Lüning, J. *Macromolecules* **2005**, *38*, 867.
(28) Chaikin, P. M.; Lubensky, T. C. *Principles of Condensed Matter Physics*; Cambridge University Press: New York, 1995; p 58.
(29) Balta-Calleja, F. J.; Vonk, C. G. *X-ray Scattering of Synthetic Polymers*; Elsevier: New York, 1989; p 297.
(30) Teixeira, J. *J. Appl. Crystallogr.* **1988**, *21*, 781.
(31) Schmidt, P. W.; Avnir, D.; Levy, D. *J. Chem. Phys.* **1991**, *94*, 1474.
(32) Ou-Yang, W. C.; Chen, H. L.; Ho, D. L.; Tsao, C.-T.; Yang, G.; Peng, K. Y.; Chen, S. A.; Han, C. C., submitted to *Phys. Rev. Lett.*
(33) Meng, H. F.; Tzeng, K. C.; Chen, B. L.; Horng, S. F.; Chang, S. M.; Hsu, C. S., submitted to *Phys. Rev. Lett.*
(34) Peng, K. Y.; Chen, S. A.; Fann, W. S. *J. Am. Chem. Soc.* **2001**, *123*, 11388.
(35) Nguyen, T. Q.; Wu, J.; Doan, V.; Schwartz, B. J.; Tolbert, S. H. *Science* **2000**, *288*, 652.
(36) Yu, J.; Hu, D. H.; Barbara, P. F. *Science* **2000**, *289*, 1327.
(37) Neher, D. *Macromol. Rapid Commun.* **2001**, *22*, 1365 and references therein.
(38) Scherf, U.; List, E. J. W. *Adv. Mater.* **2002**, *14*, 477 and references therein.
(39) Tanto, B.; Guha, S.; Martin, C. M.; Scherf, U.; Winokur, M. J. *Macromolecules* **2004**, *37*, 9438.

MA050367U